Inorg. Chem. **2005**, *44*, 17−26

Hydrogenation of Two-Electron Mixed-Valence Iridium Alkyl Complexes

Adam S. Veige,† Thomas G. Gray,‡ and Daniel G. Nocera*

Department of Chemistry, 6-335, Massachusetts Institute of Technology, 77 Massachusetts Avenue, Cambridge, Massachusetts 02139-4307

Received June 10, 2004

Two-electron mixed-valence complexes of the general formula $(tfepma)_3Ir_2^{0,II}RBr$ [tfepma = bis(bis(trifluoroethoxy)-phosphino)methylamine, $MeN[P(OCH_2CF_3)_2]_2$, and R = CH_3 (**2**), $CH_2C(CH_3)_3$ (**3**)] have been synthesized and structurally characterized and their reactivity with H_2 investigated. Hydrogenation of **2** and **3** proceeds in a cascade reaction to produce alkane upon initial H_2 addition, followed by the formation of the $Ir_2^{I,III}$ binuclear trihydride–bromide complex $(tfepma)_3Ir_2^{I,III}H_3Br$ (**4**) upon the incorporation of a second molecule of H_2. Hydrogenation of two-electron mixed-valence di-iridium alkyl complexes is examined with nonlocal density-functional calculations. H_2 attacks the Ir^{II} metal center prior to alkyl protonation to produce an η^2–H_2 complex. Transition states link all intermediates to a complex that has the same regiochemistry as the crystallographically determined final product. Calculated atomic charges suggest that the second H_2 molecule is homolytically cleaved within the di-iridium coordination sphere and that a hydrogen atom migrates across the intact Ir–Ir metal bond. These results are consistent with the emerging trend that two-electron mixed-valence cores manage the two-electron chemistry of substrates with facility when hydrogen is the atom that migrates between metal centers.

Introduction

Cooperative bimetallic reactivity is based on the premise that two metals combined might enable transformations different from those of the individual metal ions.[1−3] This concept is especially pertinent to multielectron redox design since each metal can contribute the redox equivalency accommodated within the range of normal oxidation states of the metal ion. For most coordination complexes, an oxidation change of one is typical and therefore a net two-electron process may result from cooperative bimetallic reactivity. Higher electron equivalency may be achieved if the metals can undergo multielectron changes in their oxidation number. Such is the case for digold complexes[4,5] coordinated by ylides and dirhodium[6,7] and di-iridium[8,9] complexes coordinated by diphosphazanes. In these ligand environments, the metals can react in two-electron steps to drive overall four-electron transformations. Critical to the success of intermetal redox cooperation is the two-electron mixed-valence oxidation state, $M^n\cdots M^{n+2}$, which is the linchpin that connects the two-electron chemistry of $M^n\cdots M^n$ and $M^{n+2}\cdots M^{n+2}$ redox termini.

The two-electron mixed-valence state is especially important in managing the multielectron chemistry of hydrogen activation and production. Hydrogen halides react with bimetallic phosphazanes to produce two-electron mixed-valence metal−hydrides, which undergo facile H_2 elimination.[8,10] For the case of dirhodium complexes, HX addition to a $Rh_2^{0,0}$ center produces $Rh^0-Rh^{II}X_2$ complexes and dihydrogen; the $Rh^{II}-X$ bond may be photoactivated[6,7] thus enabling a photocatalytic cycle for the production of hydrogen from homogeneous HX (X = Cl, Br) solutions.[11]

* Author to whom correspondence should be addressed. E-mail: nocera@mit.edu.

† Present address: Department of Chemistry, The University of Florida, Gainesville, FL 32611-7200.

‡ Present address: Department of Chemistry, Case Western Reserve University, 10900 Euclid Avenue, Cleveland, OH 44106-7078.

(1) Bosnich, B. *Inorg. Chem.* **1999**, *38*, 2554−62.
(2) Gavrilova, A. L.; Bosnich, B. *Chem. Rev.* **2004**, *104*, 349−84.
(3) Stanley, G. In *Catalysis by Di- and Polynuclear Metal Cluster Complexes*; Adams, R. D., Cotton, F. A., Eds.; Wiley-VCH: New York, 1998; pp 345−72.
(4) Fackler, J. P., Jr. *Inorg. Chem.* **2002**, *41*, 6959−72.
(5) Grohmann, A.; Schmidbauer, H. In *Comprehensive Organometallic Chemistry, II*; Abel, E. W., Stone, F. G. A., Wilkinson, G., Eds.; Pergamon: New York, 1995; Vol. 3, p 1.
(6) Heyduk, A. F.; Macintosh, A. M.; Nocera, D. G. *J. Am. Chem. Soc.* **1999**, *121*, 5023−32.
(7) Odom, A. L.; Heyduk, A. F.; Nocera, D. G. *Inorg. Chim. Acta* **2000**, *297*, 330−7.
(8) Heyduk, A. F.; Nocera, D. G. *J. Am. Chem. Soc.* **2000**, *122*, 9415−26.
(9) Heyduk, A. F.; Nocera, D. G. *Chem. Commun.* **1999**, 1519−20.
(10) Gray, T. G.; Veige, A. S.; Nocera, D. G. *J. Am. Chem. Soc.* **2004**, *126*, 9670−78.
(11) Heyduk, A. F.; Nocera, D. G. *Science* **2001**, *293*, 1639−41.

10.1021/ic049246l CCC: $30.25
Published on Web 12/01/2004

The facility of hydrogen activation is derived from the ability to preserve the formal two-electron mixed valency while shuttling a hydrogen atom between adjacent metals.[10] Unique reactivity is observed as a consequence of hydrogen-atom migration, including the unusual circumstance of reversible M−M bond hydrogenation without M−M bond cleavage in a bimetallic compound.

We now report the synthesis of alkyl complexes of an $Ir_2^{0,II}$ mixed-valence core and their reactivity with H_2. Hydrogenation of $Ir_2^{0,II}$ alkyl proceeds in a cascade reaction to produce alkane upon initial H_2 addition followed by subsequent H_2 addition to form a trihydride. The dihydrogen uptake reaction is examined with nonlocal density-functional calculations. Structural predispositions toward cooperative bimetallic reactivity are considered and reaction intermediates and transition states are identified and related to the known reaction chemistry of the $Ir_2^{0,II}$ alkyl complex. In addition to providing a new synthetic route to accessing hydrido−halo species, which are crucial to HX photocatalysis of two-electron mixed-valence complexes, the chemistry described herein offers an opportunity to examine how H_2 adsorption, hydrogenation of metal−alkyl bonds, and oxidative addition are facilitated by adjacent metals that are electronically and coordinatively disparate.

Experimental Section

General Procedures. All synthetic manipulations were conducted in the dry, anaerobic environment provided by a Schlenk-line or a nitrogen-filled glovebox. Solvents for synthesis were of reagent grade or better and were dried according to standard methods. The ligand precursor $MeN(PCl_2)_2$, bis(bis(trifluoroethoxy)-phosphino)methylamine (tfepma), and the di-iridium complex $(tfepma)_3Ir_2^{0,II}Cl_2$ (**1**) were prepared following published procedures.[8] The starting materials $[Ir(cod)Cl]_2$ (Strem), CH_3MgBr (Alfa Aesar), $(CH_3)_3CH_2MgCl$ (Aldrich), H_2 (BOC Gases, UHP Grade 5), and D_2 (Aldrich) were used as received.

Preparation of $(tfepma)_3Ir_2^{0,II}CH_3Br$ (2). To a solution of $(tfepma)_3Ir_2^{0,II}Cl_2$ (**1**) (500 mg, 0.261 mmol) in THF (8 mL) was added CH_3MgBr (91 μL, 3.14 M in ether, 0.288 mmol) at −35 °C. The solution turned brown upon being slowly warmed to ambient temperature. A brown oily residue remained after removing all volatile materials; a green powder resulted after triturating with CH_2Cl_2 (4 × 3 mL). To remove residual salts, the material was dissolved in CH_3CN to give a bright yellow solution, which yielded a yellow oil of the acetonitrile adduct, **2-CH$_3$CN**, upon solvent removal. The oil was taken up in CH_2Cl_2 and the solution was filtered. The filtrate was condensed (1 mL), diluted with CH_2Cl_2 (1 mL), and layered with pentane. Orange crystals of **2-CH$_3$CN** deposited after 18 h. The crystals were dried to remove coordinated CH_3CN, and **2** was obtained as a green microcrystalline powder in 40% yield (196 mg). Since **2** was only sparingly soluble in noncoordinating solvents, spectral analysis was performed on **2-CH$_3$CN**.

Analytical Data for 2-CH$_3$CN. ^{1}H NMR (500 MHz, CD_3CN, 25 °C), δ/ppm: 1.11 (dd, 8 Hz, 3 Hz, 3 H), 2.61 (t, 6 Hz, 3 H), 2.70 (m, 3 H), 2.80 (m, 3 H), 4.1−5.4 (m, 24 H). $^{31}P\{^1H\}$ NMR (202.5 MHz, CD_3CN, 25 °C) δ /ppm: 29.5 (s, 1 P), 44.8 (t, 303 Hz, 1 P), 72.5 (d, 134 Hz, 1 P), 93.8 (dm, 298 Hz, 1 P), 95.5 (dm, 310 Hz, 1 P, 109.3 (dm, 152 Hz 1 P); Anal. Calcd. for $C_{28}H_{36}N_3P_6O_{12}F_{36}BrIr_2$ (**2**): C, 17.33; H, 1.87; N, 2.17. Found: C, 16.69; H, 1.73; N, 2.15.

Preparation of $(tfepma)_3Ir_2^{0,II}NpBr$ (3). To a solution of $(tfepma)_3Ir_2^{0,II}Cl_2$ (**1**) (332 mg, 0.173 mmol) and NaBr (60 mg, 0.583 mmol) in THF (8 mL) was added $(CH_3)_3CH_2MgCl$ (253 μL, ∼0.75 M in ether) at −35 °C. Upon slowly warming to ambient temperature, the solution turned deep emerald green. After removing all volatile materials, a green oily residue remained; a green powder formed after triturating with CH_2Cl_2 (4 × 3 mL). The residual salts were removed by filtration in CH_2Cl_2 (20 mL) and a brilliant green crystalline precipitate formed from a cold filtrate (−35 °C) after 15 h. The supernatant was removed and the crystals were washed with pentane (2 × 1 mL) to give 225 g (67% yield) of **3**.

Analytical Data for 3. ^{1}H NMR (500 MHz, CD_2Cl_2, 25 °C), δ/ppm: 0.81 (m, 1 H), 0.95 (s, 9 H), 2.17 (dt, 10.0 Hz, 13.5 H, 1 H), 2.35 (dd, 11.0 Hz, 11.5 Hz, 3 H), 2.60 (m, 3H), 2.89 (bs, 3H), 3.8−4.9 (m, 24 H). $^{31}P\{^1H\}$ NMR (202.5 MHz, CD_2Cl_2, 25 °C) δ /ppm: 10.00 (bs, 1 P), 59.96 (bs, 1 P), 81.36 (m, 1 P), 102.54 (m, 2 P), 134.31 (m, 1 P). Anal. Calcd. for $C_{32}H_{44}N_3P_6O_{12}F_{36}BrIr_2$ (**3**): C, 19.25; H, 2.22; N, 2.10. Found: C, 18.40; H, 2.65; N, 2.05.

Preparation of $(tfepma)_3Ir_2^{I,III}H_3Br$ (4). Hydrogen (1 atm) was admitted to a degassed frozen solution of **3** (270 mg, 0.135 mmol) in CH_2Cl_2 (5 mL). The green solution quickly turned bright yellow upon thawing and warming to room temperature. After stirring for an additional 10 min, all volatiles were removed to yield a yellow powder. After filtration in a minimal amount of CH_2Cl_2, the filtrate was cooled to −35 °C and the supernatant was decanted. The product was isolated as a pale yellow crystalline solid in 55% yield (143 mg).

Analytical Data for 4. ^{1}H NMR (300 MHz, CD_2Cl_2, 25 °C), δ/ppm: 2.63 (t, 10 Hz, 3 H), 2.74 (t, 7 Hz, 3 H), 2.795 (m, 3 H), 3.9−5.0 (m, 24H), −10.94 (dm, 235 Hz, 1 H), −11.70 (bm, 1 H), −12.41 (dq, 139 Hz, 12 Hz, 1 H). $^{31}P\{^1H\}$ NMR (202.5 MHz, CD_2Cl_2, 25 °C) δ/ppm: 41.27 (bs, 1 P), 42.88 (bs, 1 P), 90.68 (m, 1 P), 93.51 (d, 150 Hz, 1 P), 94.81 (m, 1 P), 98.10 (m 1 P). Anal. Calcd. for $C_{27}H_{36}N_3P_6O_{12}BrF_{36}Ir_2$ (**4**): C, 16.81; H, 1.88; N, 2.18. Found: C, 16.84; H, 1.75; N, 2.10.

Physical Methods. All NMR spectra were collected at the MIT Department of Chemistry Instrumentation Facility on a Varian Inova Unity 500 spectrometer unless otherwise noted. The NMR solvents, CD_2Cl_2 and CD_3CN, were dried using appropriate agents. ^{1}H NMR spectra (500 MHz) were referenced to TMS using the residual protio impurities of the given solvent. $^{31}P\{^1H\}$ NMR spectra (202.5 MHz) were referenced to an external 85% H_3PO_4 standard. All chemical shifts are reported using the standard δ notation in parts per million; positive chemical shifts are to a higher frequency from the given reference. Elemental analyses were performed at H. Kolbe Mikroanalytisches Laboratorium and Robertson Microlit Laboratories.

X-ray Diffraction Studies. X-ray diffraction experiments were performed on single crystals grown from concentrated solutions at −35 °C or by solvent-layering techniques. Crystals were removed from the supernatant and transferred onto a microscope slide coated with Paratone N oil. Selected crystals were affixed to a glass fiber in wax and Paratone N oil and frozen in a nitrogen stream. Data collection was performed by shining Mo Kα (λ = 0.71073 Å) radiation onto crystals mounted onto a three-circle goniometer Siemens Platform equipped with a CCD detector. The data were processed and refined by using the program SAINT supplied by Siemens Industrial Automation, Inc. The structures were solved by direct methods (SHELXTL v6.10, Sheldrick, G. M. and Siemens Industrial Automation, Inc., 2000) in conjunction with standard difference Fourier techniques. All non-hydrogen atoms were refined anisotropically, unless otherwise noted. Hydrogen atoms were placed in calculated positions. Some details regarding the refined data and cell parameters are provided in Table 1.

Table 1. Selected Bond Lengths and Angles from X-ray Analysis of **2-CH_3CN**, **3** and **4**[a]

2-CH_3CN		**3**		**4**	
bond	distance/Å	bond	distance/Å	bond	distance/Å
Ir1−Ir2	2.82909(9)	Ir1−Ir2	2.7910(8)	Ir1−Ir2	2.8703(8)
Ir1−C1	2.278(11)	Ir1−C1	2.160(13)	Ir2−Br1	2.6075(18)
Ir1−Br1	2.6909(17)	Ir1−Br1	2.5191(16)	Ir2−P1	2.215(4)
Ir1−N1	2.088(11)	C1−C2	1.54(2)	Ir1−P2	2.265(3)
Ir1−P1	2.164(4)	Ir1−P1	2.165(4)	Ir2−P3	2.208(4)
Ir2−P2	2.228(4)	Ir2−P2	2.222(4)	Ir1−P4	2.254(4)
Ir1−P3	2.249(3)	Ir1−P3	2.254(4)	Ir1−P5	2.326(4)
Ir2−P4	2.224(3)	Ir2−P4	2.249(4)	Ir1−P6	2.256(4)
Ir2−P5	2.251(3)	Ir2−P5	2.211(4)		
Ir2−P6	2.220(3)	Ir2−P6	2.286(4)		
Ir1−N1−C2	170.2(11)	P3−Ir1−C1	171.6(4)	P1−Ir2−P3	170.70(11)
P1−Ir1−Br1	101.86(10)	Ir1−Ir2−P5	163.68(10)	P2−Ir1−P4	159.2(14)
Ir1−Ir2−Br1	174.27(4)	Ir2−Ir1−C1	97.5(4)	Ir1−Ir2−P6	172.70(11)
Ir1−Ir2−P6	164.52(10)	C1−Ir1−Br1	86.5(4)	P5−Ir1−Ir2	104.00(11)
P3−Ir1−C1	170.2(11)	C1−Ir1−Ir2−P6	19.6	Ir1−Ir2−Br1	91.83(4)
				P5−Ir1−P4	95.06(14)
				Br−Ir2−Ir1−P5	24.8

[a] See Figures 1, 2, and 4 for atom-numbering scheme.

X-ray Structure of (tfepma)$_3$Ir$_2^{0,II}$CH$_3$Br(CH_3CN), (2-CH_3CN). A bright orange crystal of approximate dimensions 0.49 × 0.45 × 0.35 mm^3 was obtained by layering a CH_2Cl_2/CH_3CN solution of **2-CH_3CN** with pentane. A total of 26162 reflections were collected in the θ range 2.46° to 23.28°, of which 9567 were unique (R_{int} = 0.0697). The structure was solved using direct methods with standard difference Fourier techniques. A molecule of crystallization (CH_3CN) was found within the asymmetric unit. Due to the proximity of the methyl group to the heavy atom Ir1, it could only be refined isotropically. The largest peak and hole in the difference map were 2.742 and −1.492 e Å^{-3}, respectively. The least squares refinement converged normally giving residuals of $R1$ = 0.0565, $wR2$ = 0.1363, and GOF = 1.101.

Crystal Data for $C_{32}H_{42}F_{36}Ir_2N_5O_{12}P_6Br$. Orthorhombic, $P2_12_12_1$, Z = 4, a = 13.319(3) Å, b = 20.326(4) Å, c = 24.727(5) Å, V = 6695(2) Å^3, ρ_{calc} = 2.007 g/cm^3, F(000) = 7752.

X-ray Structure of (tfepma)$_3$Ir$_2^{0,II}$NpBr (3). An emerald green crystal of approximate dimensions 0.27 × 0.07 × 0.03 mm^3 was obtained by cooling a concentrated solution of **3** to −35 °C. A total of 24939 reflections were collected in the θ range 2.20 to 23.28°, of which 8924 were unique (R_{int} = 0.0732). The structure was solved using direct methods with standard difference Fourier techniques. The largest peak and hole in the difference map were 1.963 and −2.031 e Å^{-3}, respectively. The least squares refinement converged normally giving residuals of $R1$ = 0.0724, $wR2$ = 0.1560, and GOF = 1.114.

Crystal Data for $C_{32}H_{44}F_{36}Ir_2N_3O_{12}P_6Br$. Monoclinic, $P2_1/n$, Z = 4, a = 13.6124(10) Å, b = 25.4652(19) Å, c = 18.1572(13) Å, β = 98.800(1)°, V = 6220.0(8) Å^3, ρ_{calc} = 2.132 g/cm^3, F(000) = 3824.

X-ray Structure of (tfepma)$_3$Ir$_2^{0,II}$H$_3$Br (4). A colorless crystal of approximate dimensions 0.23 × 0.08 × 0.06 mm^3 was obtained by layering a CH_2Cl_2 solution of **4** with pentane. A total of 12492 reflections were collected in the θ range 2.20° to 23.28°, of which 12492 were unique (R_{int} = 0.0376). The structure was solved using direct methods with standard difference Fourier techniques. The DFIX command was used to restrict O5−C12, O9−C20, and C16−C17. One trifluoroethoxy group was disordered and partitioned using the PART command. One crystallization solvent molecule (CH_2Cl_2) was found within the asymmetric unit. The largest peak and hole in the difference map were 1.382 and −1.632 e Å^{-3}, respectively. The least squares refinement converged normally giving residuals of $R1$ = 0.0858, $wR2$ = 0.1224, and GOF = 1.151.

Crystal Data for $C_{28}H_{38}F_{36}Ir_2N_3O_{12}P_6Br$. Triclinic, $P1$, Z = 2, a = 11.8808(9) Å, b = 12.5906(9) Å, c = 23.2466(18) Å, α = 75.3630(10)°, β = 84.2370(10)°, γ = 63.8360(10)°, V = 3019.5(4) Å^3, ρ_{calc} = 2.215 g/cm^3, F(000) = 1920.

Computational Details. Calculations were performed within the Gaussian 98 Program suite.[12] DFT computations employed the hybrid functional of Truhlar et al.,[13] which is a variant of the Perdew−Wang exchange-correlation functional[14−17] incorporating a 42.8% admixture of Hartree−Fock exchange. The default "extrafine" grid was used throughout. Self-consistent field convergence was achieved with direct methods. Equilibrium geometries were optimized in redundant internal coordinates;[18] transition state structures were computed with quadratic synchronous searching algorithms.[19] Relativistic effective core potentials were used for iridium along with the standard Hay−Wadt[20−22] double-ζ basis set, augmented by the optimized Ir 6p-function of Couty and Hall.[23] The 6-31G(d,p) basis of Pople and co-workers[24,25] was applied to all other atoms. Reported energies are sums of electronic and thermal free energies; these incorporate zero-point energies.

(12) Frisch, M. J.; Trucks, G. W.; Schlegel, H. B.; Scuseria, G. E.; Robb, M. A.; Cheeseman, J. R.; Zakrzewski, V. G.; Montgomery, J. A., Jr.; Stratmann, R. E.; Burant, J. C.; Dapprich, S.; Millam, J. M.; Daniels, A. D.; Kudin, K. N.; Strain, M. C.; Farkas, O.; Tomasi, J.; Barone, V.; Cossi, M.; Cammi, R.; Mennucci, B.; Pomelli, C.; Adamo, C.; Clifford, S.; Ochterski, J.; Petersson, G. A.; Ayala, P. Y.; Cui, Q.; Morokuma, K.; Malick, D. K.; Rabuck, A. D.; Raghavachari, K.; Foresman, J. B.; Cioslowski, J.; Ortiz, J. V.; Stefanov, B. B.; Liu, G.; Liashenko, A.; Piskorz, P.; Komaromi, I.; Gomperts, R.; Martin, R. L.; Fox, D. J.; Keith, T.; Al-Laham, M. A.; Peng, C. Y.; Nanayakkara, A.; Gonzalez, C.; Challacombe, M.; Gill, P. M. W.; Johnson, B. G.; Chen, W.; Wong, M. W.; Andres, J. L.; Head-Gordon, M.; Replogle, E. S.; Pople, J. A. *Gaussian 98*, *Revision A.9*; Gaussian, Inc.: Pittsburgh, PA, 1998.

(13) Lynch, B. J.; Fast, P. L.; Harris, M.; Truhlar, D. G. *J. Phys. Chem.* **2000**, *104*, 4811−5.

(14) Perdew, J. P. In *Electronic Structure of Solids '91*; Ziesche, P., Eschig, H., Eds.; Akademie Verlag: Berlin, 1991.

(15) Perdew, J. P.; Chevary, J. A.; Vosko, J. H.; Jackson, K. A.; Pederson, M. R.; Singh, D. J.; Fiolhais, C. *Phys. Rev. B* **1992**, *46*, 6771−87.

(16) Perdew, J. P.; Burke, K.; Wong, Y. *Phys. Rev. B* **1996**, *54*, 16533−9.

(17) Burke, K.; Perdew, J. P.; Wang, Y. In *Electronic Density Functional Theory: Recent Progress and New Directions*; Dobson, J. F., Vignale, G., Das, M. P., Eds.; Plenum: New York, 1998.

(18) Peng, C.; Ayala, P. Y.; Schlegel, H. B.; Frisch, M. J. *J. Comput. Chem.* **1996**, *17*, 49−56.

(19) Peng, C.; Schlegel, H. B. *Israel J. Chem.* **1993**, *33*, 449−54.

(20) Hay, P. J.; Wadt, W. R. *J. Chem. Phys.* **1985**, *82*, 270−83.

(21) Hay, P. J.; Wadt, W. R. *J. Chem. Phys.* **1985**, *82*, 284−98.

(22) Hay, P. J.; Wadt, W. R. *J. Chem. Phys.* **1985**, *82*, 299−310.

Scheme 1

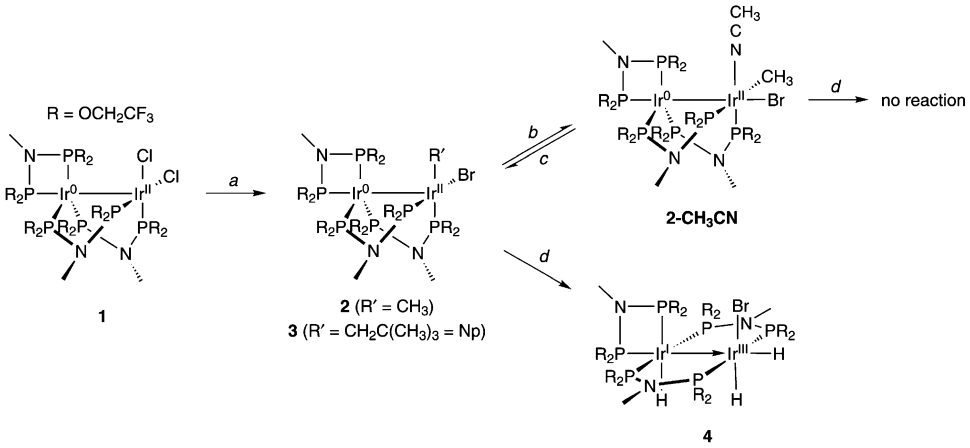

(a) For **2**: R´MgBr, THF; For **3**, R´MgBr, NaBr, THF; (b) For **2**; CH_3CN; (c) vacuum; (d) H_2 (1 atm)

Thermodynamic quantities were computed at 298 K and 1 atm, using unscaled vibrational frequencies. The minimum of the electronic energy hypersurface is used to compute vibrational partition functions, and all electronic excited states are assumed to be energetically inaccessible. Translational entropy changes that accompany changes in the number of moles of gases during the reaction are included. We report herein gas-phase calculations, and no attempt has been made to correct for the nonideality of gases, nor for effects of solvation. All calculations were spin-restricted, and geometry optimizations proceeded without imposed symmetry.

Results

Syntheses. Simple organometallic complexes of that $Ir_2^{0,II}$ core are hitherto unknown. Alkyl complexes are obtained by applying the straightforward methodology of Scheme 1. Tetrahydrofuran solutions of **1** at low temperature cleanly react with MeMgBr to form green $(tfepma)_3Ir_2^{0,II}MeBr$ (**2**), eq 1. The inclusion of bromide ion stems from Cl^- substitution at the Ir^{II} center. A yellow solution is obtained when **2** is dissolved in CH_3CN and the orange product, $(tfepma)_3Ir_2^{0,II}MeBr(CH_3CN)$ (**2-CH_3CN**), is isolated by solvent removal. Coordination of CH_3CN appreciably increases the solubility of the metal complex, though both **1** and **2** are sparingly soluble in most noncoordinating solvents. The CH_3CN may be removed by prolonged exposure to vacuum and **2** reforms.

Three distinct $N-CH_3$ resonances in the ^1H NMR spectrum of **2-CH_3CN** indicate a low symmetry complex. Consistent with this supposition, the $^{31}P\{^1H\}$ spectrum of **2-CH_3CN** displays a characteristic spread of six phosphorus signals for a C_1 symmetric complex. Two upfield resonances at 29.5 ppm (s, 1 P) and 44.8 ppm (t, 303 Hz, 1 P) are assigned to the Ir^{II} coordinated phosphorus nuclei and a distinctly downfield shifted resonance at 109.3 ppm is assigned to the axially coordinated phosphorus nuclei of the chelating ligand. The resonances for the phosphorus atoms that form a trigonal plane about the Ir^0 center are found at 72.5, 93.8, and 95.5 ppm, of which the latter two can be assigned to the bridging ligands. The $Ir-CH_3$ protons appear upfield as a doublet of doublets at 1.11 ppm (J_{PH} = 8,Hz, J_{PH} = 3 Hz).

The X-ray crystal structure of **2-CH_3CN**, shown in Figure 1, is structurally similar to CH_3CN adducts of the $Ir_2^{0,II}$ core coordinated by simple monoanionic ligands.[8] Table 1 lists selected metrical parameters for the structure. The unsymmetrical bimolecular core consists of a trigonal bipyramidal Ir^0 center and an octahedral Ir^{II} center separated by a long Ir−Ir bond of 2.8290(9) Å. Ir−P bond lengths in axial and equatorial positions of the trigonal bipyramid of Ir^0 are very similar and only vary by 0.031 Å (2.220(3) to 2.251(3) Å), with the longest being axial. The crystal structure solution allows for the absolute assignment of an axially bound bromide ion to the Ir^{II} center with an Ir−Br bond distance of 2.6909(17) Å. This bond distance is too long for an Ir−Cl bond and refinement statistics only improved when the model contained a bromine atom. CH_3CN binds in an equatorial position (d(Ir1−N1) = 2.088 Å) and is nearly coplanar (∠N1−Ir1−Ir2−P5 = 20.1°) with the chelating ligand bound to the Ir^0 center. Two bridging-ligand phos-

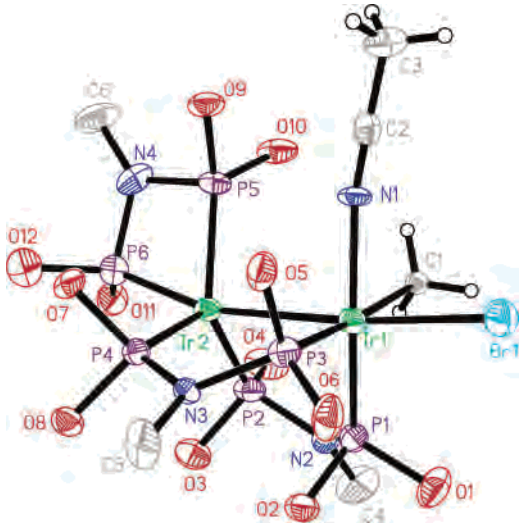

Figure 1. Solid-state structure of $(tfepma)_3Ir_2^{0,II}CH_3Br(CH_3CN)$ (**2-CH_3CN**) with thermal ellipsoids drawn at the 50% probability level and CF_3CH_2 groups removed for clarity. Not shown is a CH_3CN molecule of crystallization.

(23) Couty, M.; Hall, M. B. *J. Comput. Chem.* **1996**, *17*, 1359−70.
(24) Hariharan, P. C.; Pople, J. A. *Theor. Chim. Acta* **1973**, *28*, 213−22.
(25) Francl, M. M.; Pietro, W. J.; Hehre, W. J.; Binkley, J. S.; Gordon, M. S.; DeFrees, D. J.; Pople, J. A. *J. Chem. Phys.* **1982**, *77*, 3654−5.

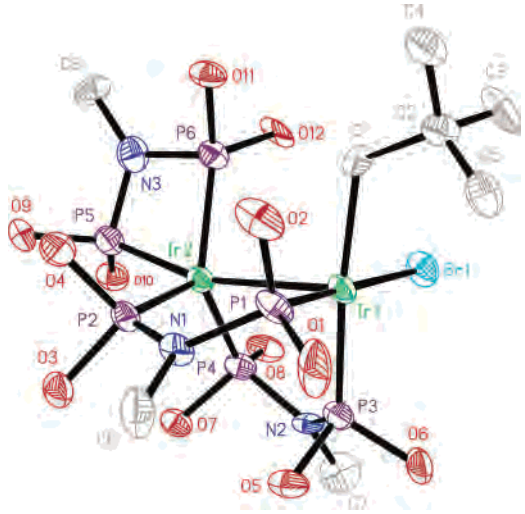

Figure 2. Solid-state structure of $(tfepma)_3Ir_2^{0,II}NpBr$ (**3**) with thermal ellipsoids drawn at the 50% probability level and CF_3CH_2 groups removed for clarity.

phorus termini (d(Ir1−P1) = 2.164(4) and d(Ir1−P3) = 2.249 Å) and the methyl group (d(Ir1−C1) = 2.278(11) complete the octahedral coordination sphere of the Ir^{II} center.

A larger alkyl derivative was sought and neopentyl was chosen so as to avoid any complications resulting from β-hydrogen elimination. The bromide complex is most easily obtained by treating **1** with NpMgCl in THF at −35 °C and using NaBr as a Br^- ion source. Unlike **1** and **2**, **3** is soluble in CH_2Cl_2; in THF, the emerald green color of the complex is preserved upon dissolution, whereas **1** and **2** turn auburn and yellow, respectively, upon dissolution in THF. Presumably, the sterically cumbersome neopentyl group does not allow THF to coordinate in contrast to its methyl congener. Conversely, yellow solutions of **3** result when the compound is dissolved in CH_3CN; presumably the smaller cylindrical CH_3CN may access the bimetallic core in a coordination fashion that is similar to **2**.

Two diastereotopic methylene protons of the neopentyl group are observed in the ^{1}H NMR spectrum of **3** at 0.81 ppm and 2.17 ppm, and a corresponding singlet for the three equivalent methyl groups. As observed for **2-CH$_3$CN**, three distinct N−CH_3 resonances are found for the C_1 symmetric complex. The X-ray structure of **3** (Figure 2) is consistent with the solution-phase structural assignment; selected bond lengths and angles can be found in Table 1. The familiar ligand environment of an $Ir_2^{0,II}$ core is observed in which two tfepma ligands bridge the metal centers and a third ligand chelates the reduced Ir^0 metal creating a nearly trigonal bipyramid arrangement. Only a slight deviation of the ∠Ir1−Ir2−$P5_{ax}$ (163.68(15)°) angle away from linearity is observed but is necessary to accommodate the chelation. The Ir^{II} site has a basal arrangement of ligands in a square plane and is capped with an Ir−Ir bond (2.7910(8) Å) at an apical position. The Ir−P bond distances (d(Ir−P)$_{avg}$ = 2.23 (4) Å) do not correlate with metal oxidation state, though the shortest bond, Ir1−P1 = 2.165 (4) Å, is consistent with a contracted Ir^{II} center. The coordination spheres of the $Ir_2^{0,II}$ core are slightly twisted as signified by the dihedral angle

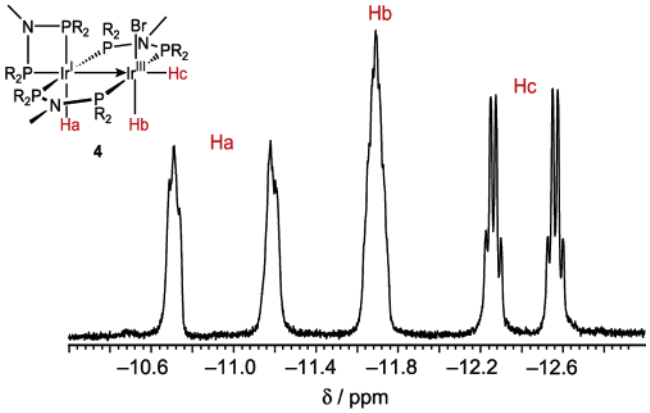

Figure 3. ^{1}H NMR spectrum depicting the hydride region of $(tfepma)_3Ir^I$-$HIr^{III}H_2Br$ (**4**). Spectrum obtained using a Varian 500 MHz spectrometer and CD_2Cl_2.

∠C1−Ir1−Ir2−P6 = 19.6°. The nearest Ir^{II}−H bonding interaction with the neopentyl group is too long (2.8 Å) to be considered agostic, though the CMe_3 group orients in a nearly eclipsed fashion (∠Ir1−C1−C2−C5 = 27.4°) which provides a shorter Ir−H interaction than that obtained for a perfectly staggered conformation of the neopentyl group.

Hydrogen Reactivity. ^{1}H NMR (CD_2Cl_2) spectroscopy establishes that neopentane is rapidly generated upon treatment of **3** with 1 atm H_2(g). No intermediates are observed prior to the formation of the final product, a tri-hydride of composition $(tfepma)_3Ir^IHIr^{III}H_2Br$ (**4**) (see Scheme 1). We depict **4** as a mixed-valence $Ir^I \rightarrow Ir^{III}$ species possessing a dative metal−metal bond; alternatively **4** may be represented as an $Ir^{II}-Ir^{II}$ species with a discrete metal−metal bond. The relative positions of the coordinated hydrides about the metal core in **4** are discerned with the ^{1}H NMR spectrum of the complex shown in Figure 3. Three upfield resonances indicate a hydride (Ha) trans to phosphorus on Ir^I (−10.94, dm, 235 Hz), a hydride (Hb) cis to phosphorus on the Ir^{III} center (−11.70, bm), and a hydride (Hc) on the Ir^{III} center and trans to phosphorus along the axis of the metal−metal bond (−12.41, dq, 139 Hz, 12 Hz). Symmetry arguments suggest that the N−CH_3 groups of both bridging tfepma ligands should be equivalent, but three different resonances (2.63, t, 10 Hz, 3 H; 2.74, t, 7 Hz, 3 H; 2.795 m, 3 H) are detected. Only by imposing a twist angle between the two metal centers can the symmetry be lowered from C_s to C_1 providing the methyl protons with two different environments.

The twist about the metal−metal axis of **4** is observed in the single-crystal X-ray structure of the complex (Figure 4). Two bridging phosphazanes span the binuclear core and are opposite to each other, and a chelating phosphazane at the Ir^I center is preserved. A large dihedral angle (∠P5−Ir1−Ir2−Br1 = 24.8°) across the Ir1−Ir2 bond length of 2.8703(8) Å clearly forces the methyl groups of the bridging phosphazanes into two different environments. Both metal centers have octahedral coordination spheres, which is typical for metal−metal bonded d^9 and d^7 iridium centers. The proximity of the hydrogen atoms to the heavy iridium nuclei precludes the location of the hydrides but the conspicuously vacant coordination sites trans to P5 (∠P2−Ir1−P4 =

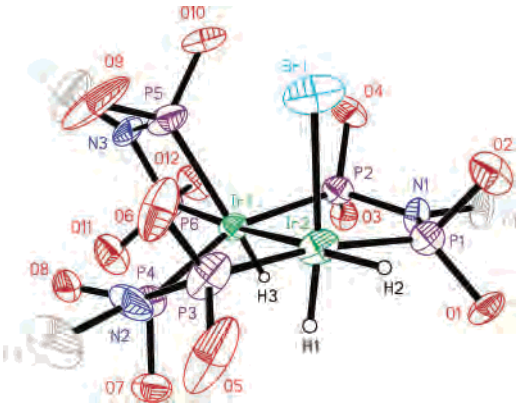

Figure 4. Solid-state structure of $(tfepma)_3Ir^{I}HIr^{III}H_2Br$ (**4**) with thermal ellipsoids drawn at the 50% probability level and CF_3CH_2 groups removed for clarity. Not shown is a CH_2Cl_2 molecule of crystallization.

159.20(14)°), cis to P1 and P3 (∠P1−Ir2−P3 = 170.72(14)°) and axially trans to P6 corroborate the aforementioned ^{1}H NMR assignments.

With spectral signatures of **4** in hand, the hydrogenation of **2** and **2-CH$_3$CN** are conveniently monitored by ^{1}H NMR spectroscopy. No color or spectral changes are observed when 1 atm of H_2 is admitted at room temperature to an NMR tube containing **2-CH$_3$CN** (Scheme 1). Only after heating the tube at 65 °C for 1.5 h did a reaction take place. A ^{1}H NMR spectrum reveals multiple resonances in the hydride region between −10 ppm and −15 ppm of which approximately 30% are attributed to **4**. In contrast, treatment of the unsolvated complex **2** in CD_2Cl_2 with H_2 at room-temperature results in a clean and prompt conversion to **4**. These results imply that initial attack of hydrogen occurs at the Ir^{II} center and an open coordination site at the metal is a requisite for reaction.

Calculations. The reaction of $Ir_2^{0,II}$ alkyls with dihydrogen was examined with nonlocal density-functional calculations within the structural and reactivity constraints imposed by the foregoing experimental studies. Chart 1 collects line drawings of model compounds, where fluorine atoms substitute for trifluoroethoxy groups on phosphorus, and hydrogens replace *N*-methyl groups. Table 2 compares calculated heavy-atom bond lengths in models **A** and **J** to experimental metrics of the authentic compounds **3** and **4**, respectively. Agreement between calculated and observed geometries, including the dihedral twist about the di-iridium bond (∠P5−Ir1−Ir2−Br1 = 24.8° (obs) vs 28.3° (calcd)), validates the models as credible representations of the actual compounds. Harmonic frequency calculations find the optimized structures **A** and **J** to be potential-energy minima.

In neopentyl complex **A**, the calculated Ir−Ir bond distance is 0.043 Å shorter than the crystallographic value observed in **3**; the disagreement between model trihydride **J** and **4** is 0.022 Å, with the calculated bond length being too short. This level of accuracy compares favorably with bond lengths calculated between fifth-period atoms using all-electron basis sets or pseudopotentials.[26−30] Inspection of calculated intraligand and metal−ligand bond lengths indicates an overbinding tendency, with calculated bond distances being ≤0.043 Å too short on a root-mean-square basis. The calculated enthalpy change of hydrogenation reaction 1

$$\mathbf{A} + 2H_2 \rightarrow \mathbf{J} + CMe_4 \qquad (1)$$

is −212.6 kJ mol^{-1}; its free energy change is −188 kJ mol^{-1}. Similar figures pertain to reaction 2

$$\mathbf{A'} + 2H_2 \rightarrow \mathbf{J} + CH_4 \qquad (2)$$

with an enthalpy change calculated to be −192.8 kJ mol^{-1}, and a free energy change of 162 kJ mol^{-1}. Both reactions are predicted to be strongly exergonic, in agreement with their experimental irreversibility. The calculations also accord with the notion that those reactions that minimize steric congestion at transition metal centers are favorable.[31,32]

The potential energy diagram in Figure 5 summarizes the proposed course of the hydrogenation reactions 1 and 2. All energies thereon are sums of electronic and thermal free energies. Computed energies are normalized to a common scale, where the combined energies of neopentyl complex **A** plus two hydrogen molecules, all at infinite separation, constitute the zero of energy. Free energies of structures **E**−**J** not having an alkane equivalent are adjusted to include the calculated energy of free neopentane, or of methane, as appropriate.

The greater steric congestion of the neopentyl complex is reflected by its destabilized ground state **A** as compared to that of the methyl complex **A′**. As suggested by the observations shown in Scheme 1, an incoming H_2 molecule attacks the alkyl bearing Ir^{II} center. Frequency calculations confirm that structures **B** and **B′** are potential-energy minima. In these structures, dihydrogen is η^2-bound at the axial coordination site of Ir^{II}. Attempts to locate analogous minima having H_2 bound to Ir^0 failed; in all cases, H_2 dissociated intact and the metal complex was unperturbed. Similarly, searches for minima or transition states corresponding to 1,2-addition of H_2 across the Ir−Ir bond failed. Structure **B** is 10.7 kJ mol^{-1} less stable than separated **A** and H_2. The analogous structure **B′** is 13.3 kJ mol^{-1} less stable than **A′** and H_2. Both energies reflect greater steric congestion resulting from the completion of the octahedral coordination geometry about the Ir^{II} center in **B** and **B′**.

Transition states **C** and **C′** are energy maxima for formal protonation of the alkyl group by η^2-H_2. Frequency calculations confirm **C** and **C′** to be saddle points of the potential energy hypersurface. Intrinsic reaction coordinates link **B** → **C** → **D** and **B′** → **C′** → **D′**, respectively. Structure **C** lies 29.8 kJ mol^{-1} higher in free energy than the separated reactants **A** + 2H_2, and **C′** is 44.9 kJ mol^{-1} more energetic than **A′** + 2H_2. Models **B** and **C** bear the two most sterically

(26) Niu, S.; Hall, M. B. *J. Am. Chem. Soc.* **1999**, *121*, 3992−9.
(27) Cotton, F. A.; Gu, J.; Murillo, C. A.; Timmons, D. J. *J. Chem. Soc., Dalton Trans.* **1999**, 3741−5.
(28) Gagliardi, L.; Roos, B. O. *Inorg. Chem.* **2003**, *42*, 1599−603.
(29) Niu, S.; Hall, M. B. *Chem. Rev.* **2000**, *100*, 353−405.
(30) Hall, M. B.; Fan, H.-J. *Adv. Inorg. Chem.* **2003**, *54*, 321−49.
(31) Stoutland, P. O.; Bergman, R. G.; Nolan, S. P.; Hoff, C. D. *Polyhedron* **1988**, *7*, 1429−40.
(32) Bryndza, H. E.; Fong, L. K.; Paciello, R. A.; Tam, W.; Bercaw, J. E. *J. Am. Chem. Soc.* **1987**, *109*, 1444−56.

Chart 1

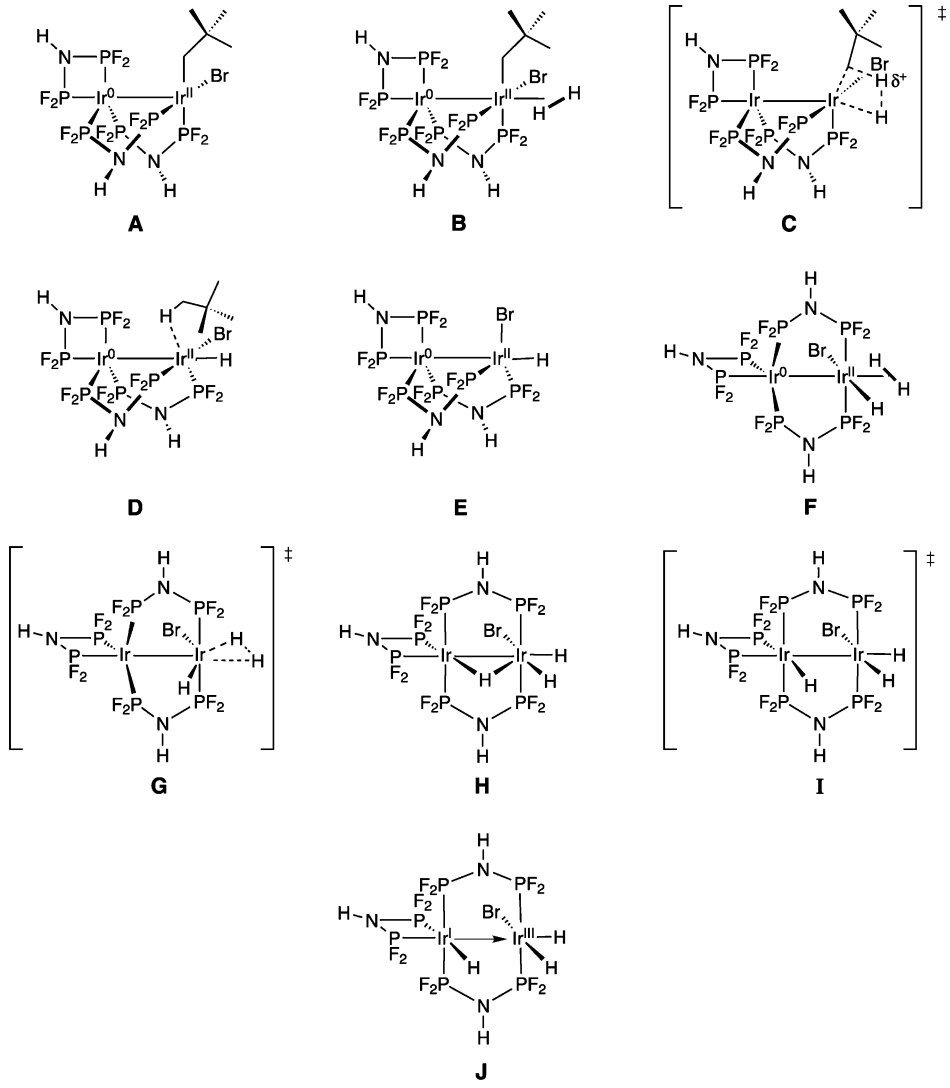

Table 2. Calculated Bond Lengths (selected) of **A** and **J** and Corresponding Distances Observed in **3** and **4**, Respectively[a]

3 and **A**			**4** and **J**		
bond pair	*d*(calc)/Å	*d*(obs)/Å[a]	bond pair	*d*(calc)/Å	*d*(obs)/Å[a]
Ir1−Ir2	2.748	2.7910(8)	Ir1−Ir2	2.892	2.8703(8)
Ir2−P2	2.202	2.222(4)	Ir1−P1	2.231	2.265(3)
Ir2−P4	2.233	2.249(4)	Ir1−P4	2.223	2.256(4)
Ir2−P5	2.208	2.211(4)	Ir1−P5	2.323	2.326(3)
Ir2−P6	2.273	2.286(4)	Ir1−P6	2.259	2.256(4)
Ir1−Br1	2.419	2.5191(16)	Ir2−Br1	2.587	2.6075(18)
Ir1−P1	2.156	2.165(4)	Ir2−P5	2.206	2.215(4)
Ir1−P3	2.250	2.254(4)	Ir2−P3	2.201	2.208(4)
Ir1−C1	2.100	2.160(13)			
rms dev.	0.043			0.010	
av. dev.	−0.030			−0.010	

[a] See Figures 2 and 4 for atom-numbering schemes.

hindered Ir^{II} centers encountered in this work. Mulliken electrostatic charges of the attacking hydrogens (not shown) are essentially unchanged along both reaction sequences, indicating a homolytic H_2 dissociation. This result is consistent with common electronegativity scales, which dictate that the Ir−H and Ir−C bonds are nearly nonpolar.[33,34]

Activated complex **C** decays to alkane complex **D**, and **C′** decays correspondingly to **D′**; both alkane complexes are energy minima. With correction for basis set superposition error,[35,36] **D** is 59.9 kJ mol^{-1} more stable than **C**, and 30.1 kJ mol^{-1} more stable than separate **A** + H_2; **D′** is 48.2 kJ mol^{-1} more stable than **C′** and 3.3 kJ mol^{-1} below **A′** + $2H_2$. In structure **D**, a neopentane approaches Ir^{II} at a distance of 1.910 Å. In **D′**, the nearest contact between Ir^{II} and a methane hydrogen is 1.974 Å. The energies of **D** and **D′** are corrected for basis set superposition error. The nearly equal energies for **D** and **D′** suggest substantial relief of the steric hindrance brought about by the alkyl ligands.

Removal of alkane from **D** and **D′** and subsequent geometry optimization produces the same complex, $Ir^{0,II}{}_2$ hydrido-bromide **E**, which a frequency calculation finds to be a minimum. The adiabatic potential energy hypersurface surrounding **E** is quite flat and optimizations have produced several structures, all closely similar to **E**, all virtually isoenergetic, and all minima. An Ir^0−Ir^{II}−Br bending vibra-

(33) Pauling, L. *The Nature of the Chemical Bond*, 3rd ed.; Cornell University Press: Ithaca, NY, 1960.
(34) Allred, A. L.; Rochow, E. G. *J. Inorg. Nucl. Chem.* **1961**, *20*, 167−70.
(35) Boys, S. F.; Bernardi, F. *Mol. Phys.* **1970**, *19*, 553−66.
(36) Gutowski, M.; Chalasinski, G. *J. Chem. Phys.* **1993**, *98*, 5540−54.

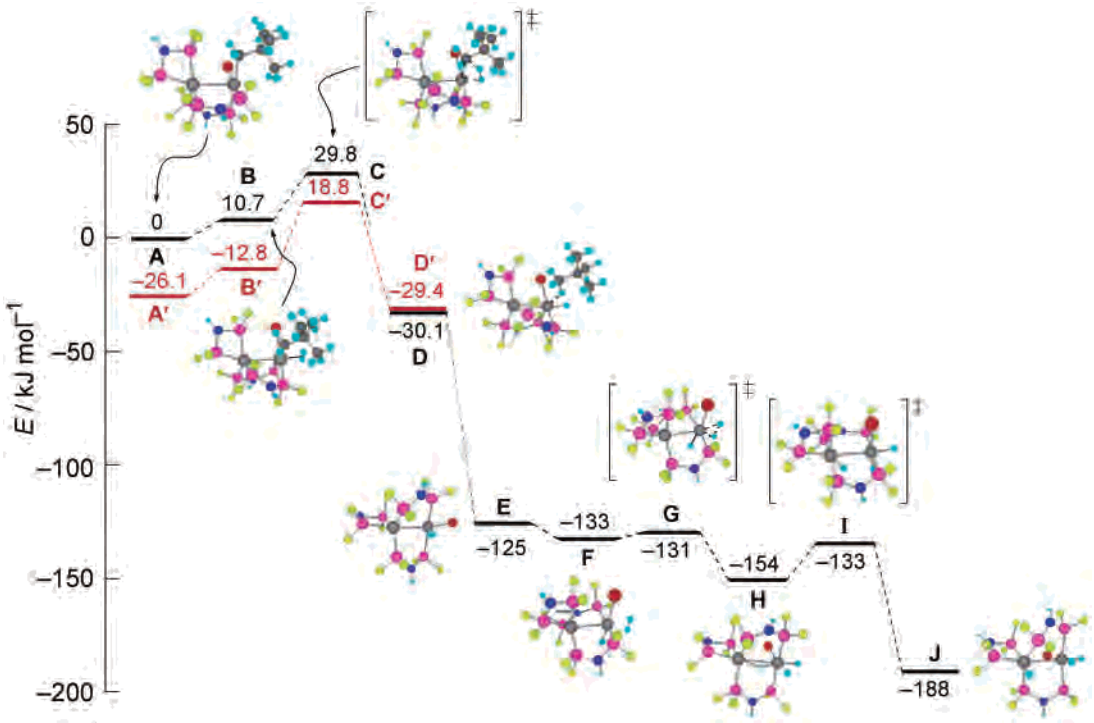

Figure 5. Potential energy diagram relating compounds involved in the model alkane elimination reaction **A** + $2H_2$ → **J** + CMe_4 (eq 1) and **A′** + $2H_2$ → **J** + CH_4 (eq 2). Energies of methyl complexes appear in red. Optimized structure of the neopentyl complex and its hydrogenation products are shown; numbering schemes appear in the Supporting Information. Sums of electronic and thermal free energies are indicated; that of **D** is corrected for basis set superposition error.

tion is calculated at 19 cm^{-1}, implying that a slight energy input elicits a large bending deformation. Indeed, the different structures calculated for intermediate **E** differ almost entirely in the position of the bromine ligand. The loss of neopentane (**D** → **E**) accounts for half of the energy expelled in reaction 1, an indication that its primary driving force is steric alleviation. Methane loss (**D′** → **E**) supplies nearly 60% of the driving force of **A′** hydrogenation. This larger fraction reflects the steric destabilization of **A** by its neopentyl group, causing compound **A** to start out at higher energy than **A′**.

The hydrogenation of the hydrido-bromide proceeds smoothly and the overall reaction proceeds by traversing **E** → **J**. Compound **F**, which is an energy-minimum, is an η^2-H_2 adduct of the Ir^{II} hydrido−bromide complex produced upon alkyl elimination. The H−H bond is substantially lengthened; the calculated bond distance is 0.905 Å compared to the distance of 0.731 Å calculated for free H_2. Dihydrogen adduct **F** is 8 kJ mol^{-1} more stable than **A** + $2H_2$ − CMe_4, all at infinite separation.

In transition state **G**, the distance between H29 and H30 has increased to 1.241 Å; all three hydrogens ligate the nonchelated iridium. The vibrational amplitude associated with the 519.5i cm^{-1} frequency is confined to the three metal-bound hydrogens, with H28 approaching Ir^0; and H29 and H30 moving apart, in motions emphasized in Figure 6. Activated complex **G** lies 2 kJ mol^{-1} higher in energy than **F**, and is 23 kJ mol^{-1} more energetic than **H**, indicating that hydrogen migration across the Ir−Ir core is essentially barrierless. Such a trend has been noted previously.[9]

In intermediate **H**, H28 bridges the two iridium centers. Structure **H** is qualitatively similar to **G**, with the only

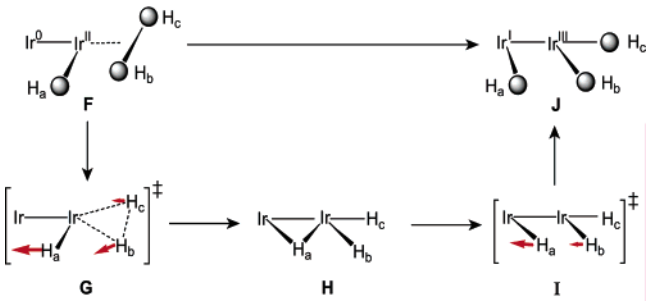

Figure 6. Calculated motions of the hydrogen ligands along the sequence **F**→**J**. Transition states are indicated in brackets; other molecular structures correspond to potential-energy minima. The red arrows in activated complexes correspond to atomic motions in the imaginary-frequency vibrations.

interesting difference being the position of one hydrogen that is bridging in **H**. The metal−metal separation in **H** is 2.939 Å, which indicates that the Ir−Ir bond is preserved, though lengthened. Inspection of metal-dominated orbitals near the frontier shows that the Ir−Ir σ-bonding combination is occupied, and the antibonding combination is vacant (it is the LUMO), consistent with direct metal−metal interaction. Structure **H** is a minimum, and it is 154 kJ mol^{-1} more stable than separated **A** + $2H_2$ − CMe_4, and 34 kJ mol^{-1} less stable than product **J**. Transition state **I** links bridged intermediate **H** with the final trihydride **J**. Compound **I** possesses a single imaginary frequency at 652i cm^{-1}, with most of the vibrational amplitude concentrated in H28, as indicated in Figure 6. Structure **I** is 21 kJ mol^{-1} more energetic than intermediate **H**, and 55 kJ mol^{-1} less stable than **J**. An intrinsic reaction coordinate links **H** → **I** → **J**. Mulliken atomic charges indicate that the hydride ligands across **H**

Scheme 2

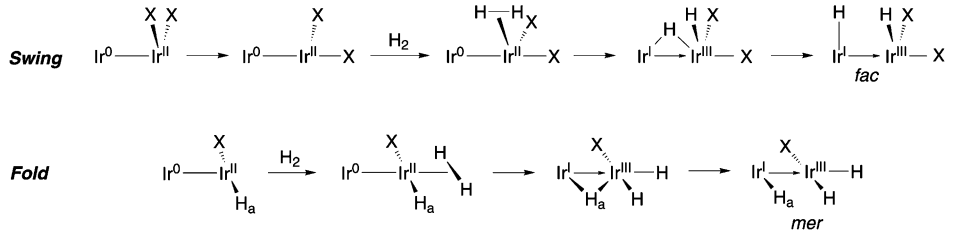

→ **I** → **J** never accumulate appreciable charge, and the reaction sequence may be best described as a homolytic splitting of H_2 in the dimetal coordination sphere.

Discussion

Hydrogenation reactions of metal−alkyls are thermodynamically driven by C−H bond formation and alkane release. As shown in Figure 5, these two processes encompass most of the driving force for the hydrogenation of the $Ir_2^{0,II}$ alkyls. The subsequent hydrogenation of the alkyl elimination product, $Ir^0-Ir^{II}(H)(X)$, proceeds under nearly thermoneutral conditions, as has been observed previously for $Ir^0-Ir^{II}X_2$ cores. The presence of an initial rate-determining barrier for the formation of the $Ir^0-Ir^{II}(R)(\eta^2\text{-}H_2)$ complex results in a cascade reaction for H_2 addition and reaction. Consistent with this computational result, treatment of **3** with precisely one equivalent of H_2 led to 50% formation of **4** with no trace of an intermediate.

The reaction sequence described in Figure 5 conforms to an emerging picture for H_2 reactivity and management at $M^n\cdots M^{n+2}$ cores. H_2 attack occurs at the Ir^{II} end of the $M^n\cdots M^{n+2}$ core for several reasons. First, H_2 reaction at the Ir^0 center is prevented by its $18e^-$ count. Were one arm of the chelating ligand to detach, the Ir^0 center would have an electron count of $16e^-$, and might bind H_2; however, we have shown previously that dissociation of the phosphazane is energetically prohibitive.[10] Second, we have never located intermediates or transition states compatible with a 1,2-addition across the Ir−Ir bond. Finally, oxidative addition to produce a $Ir^0-Ir^{IV}(H)_2$ dihydride does not appear to be germane to the two-electron mixed-valence chemistry as geometry optimization of such species collapses to η^2-H_2 complexes. The confluence of these effects directs H_2 attack at the coordinatively and electronically ($16e^-$) unsaturated Ir^{II} center.

η^2-H_2 may associate to the Ir^{II} center in axial or equatorial coordination sites. For the latter to occur, an equatorial ligand must rotate into an axial position. This conformational change has been observed both experimentally[8] and computationally[10] to be energetically costly, on the order of ∼100 kJ mol^{-1}. For $Ir_2^{0,II}$ alkyls, lower energy pathways confront H_2 reactivity from the axial coordination site without the need for rearrangement of the primary coordination sphere of the Ir^{II} center. The charge distribution of the hydrogen suggests homolytic cleavage and accordingly alkane elimination bears similarities to σ-bond metathesis, though the reaction may be more sensibly described as a protonation of the bound alkyl. Hydrogen reaction with the hydrido−halo product of dealkylation, $Ir^0-Ir^{II}(H)(Br)$, is also initiated from the axial coordination site of the Ir^{II} alkyl. H_2 may sweep across the metal−metal bond (see Figure 6). Addition with this stereochemistry yields a final product in which the monoanionic ligands assume a *mer* arrangement on the Ir^{III} center (see Scheme 2), in contrast to H_2 reaction from an equatorial coordination site at the Ir^{II} center to give a *fac* disposition of monoanionic ligands.

The specific pathways and resulting stereochemistry for H_2 addition to $Ir_2^{0,II}$ cores are summarized in Scheme 2. We believe that addition pathways labeled "swing" and "fold" are governed by the hydrogen atom migration. Addition of H_2 to the axial site of $Ir^0-Ir^{II}(X)_2$ cores is nonproductive. To position a hydrogen atom for transfer to the neighboring Ir^0 center, an equatorial ligand must swing into the axial coordination site. Once residing in the equatorial coordination site, a hydrogen atom may easily migrate into a position bridging the two iridium centers to give the desired transition state for H_2 activation. A similar bridge state for hydrogen atom migration at $Ir^0-Ir^{II}(H)(X)$ cores may be attained without the need for significant ligand re-distribution; axial ligands of the Ir^{II} center are highly mobile (**E** → **F**) and they are easily able to move out of the way of an incoming ligand. The terminal hydride (H_a in Scheme 2) that is present from the outset may smoothly fold into the bridging position as hydrogen attacks the axial coordination site. Thus the hydrogen atom is able to traverse the di-iridium core without the need for an energetically costly rotation of a terminal ligand from an equatorial site. The proposed model depicted in Scheme 2 possesses a certain predictive power. The reaction of HX with $Ir^0-Ir^{II}(X)_2$ cores is expected to occur in accordance with a swing mechanism to yield a $(H)Ir^I\rightarrow Ir^{III}(X)_3$ product with a *fac* stereochemistry. This is the observed result.[8]

We note that the addition reaction through a hydride bridge transition state is akin to that for the microscopic reverse reaction, dinuclear elimination. Some metal hydrides, which exhibit sluggish intramolecular elimination, are known to be extremely unstable in the presence of a second complex capable of attaining coordinative unsaturation. The enhanced reactivity has been ascribed by Norton to the following transformation:[37−39]

(3)

where R is hydride, alkyl, or acyl. Dinuclear elimination is only possible when at least one of the ligands is hydride, which must migrate to the bridging position for elimination

(37) Norton, J. R. *Acc. Chem. Res.* **1979**, *12*, 139−45.

to occur. For the case of the mixed-valence compounds, the coordinative unsaturation and hydride are already present. With neighboring metals of a $M^{n}\cdots M^{n+2}$ core working in concert, the hydrogen atom migrates to and from the critical bridging position to promote facile H_2 addition (as described here) and H_2 elimination,[10] respectively. Essential for H_2 reactivity at $M^{n}\cdots M^{n+2}$ cores appears to be the ability of the ligand framework to maintain the electronic and steric asymmetry of the two-electron mixed-valence core without excessive reorganization as the hydrogen migrates among terminal and bridging coordination sites. Taken together, the results of $Ir^{0}-Ir^{II}(X)_2$ and $Ir^{0}-Ir^{II}(X)(H)$ cores described herein show that the two-electron chemistry attendant to H_2 attack, activation, and migration can be managed with facility at two-electron mixed-valence cores.

(38) Martin, B. D.; Warner, K. E.; Norton, J. E. *J. Am. Chem. Soc.* **1986**, *108*, 33−39.
(39) Kristjánsdóttir, S. S.; Norton, J. A. In *Transition Metal Hydrides*; Dedieu, A., Ed.; VCH: New York, 1990; Chapter 9.

Acknowledgment. The National Science Foundation (Grant CHE-0132680) funded this research. T. G. G. acknowledges a postdoctoral fellowship from the National Institutes of Health.

Supporting Information Available: X-ray crystal structure solutions of **2-CH$_3$CN**, **3**, and **4** (pdf). This material is available free of charge via the Internet at http://pubs.acs.org.

IC049246L